GDCh
Research Article
Angewandte
International Edition Chemie
www.angewandte.org

How to cite: *Angew. Chem. Int. Ed.* **2024**, *63*, e202411418
doi.org/10.1002/anie.202411418

Self-Healable Ionic Elastomers

A Soft, Fatigue-free, and Self-healable Ionic Elastomer via the Synergy of Skin-like Assembly and Bouligand Structure

Xinyuan Jiang+, Yin Cheng+, Liangjing Shi, Jing Sun, and Ranran Wang**

Abstract: Soft ionic elastomers that are self-healable, fatigue-free, and environment-tolerant are ideal structural and sensing materials for artificial prosthetics, soft electronics, and robotics to survive unpredictable service conditions. However, most synthetic strategies failed to unite rapid healing, fatigue resistance, and environmental robustness, limited by their singular compositional/structural designs. Here, we present a soft, tough, fatigue-resistant, and self-healable ionic elastomer (STFSI elastomer), which fuses skin-like binary assembly and Bouligand helicoidal structure into a composite of thermoplastic polyurethane (TPU) fibers and a supramolecular ionic biopolymer. The interlocked binary assembly enables skin-like softness, high stretchability, and strain-adaptive stiffening through a matrix-to-scaffold stress transfer. The Bouligand structure contributes to superhigh fracture toughness ($101.6\,\mathrm{kJ\,m^{-2}}$) and fatigue resistance ($4937\,\mathrm{J\,m^{-2}}$) via mechanical toughening by interlayer slipping and twisted crack propagation path. Besides, the STFSI elastomer is self-healable through a "bridging" method and environment-tolerant ($-20\,^{\circ}\mathrm{C}$, strong acid/alkali, saltwater). To demonstrate the versatile structural and sensing applications, we showcase a safety cushion with efficient damping and suppressed rebounding, and a robotic sensor with excellent fatigue crack tolerance and instant sensation recovery upon cutting-off damage. Our presented synthetic strategy is generalizable to other fiber-reinforced tough polymers for applications involving demanding mechanical/environmental conditions.

Introduction

Soft human skin-like materials, which mimic the unparalleled combinatory merits of strain-stiffening behavior, high toughness and fatigue resistance, self-healing ability, and mechano-sensitivity, have been intensively pursued as they are uniquely suitable for applications of human-machine interfaces,[1] artificial prosthetics,[2] soft electronics[3] and robotics.[4] The mechanoreceptors (e.g., Merkel's disk and Ruffini ending) embedded under the epidermis help to perceive the environmental mechanical stimuli; Dermis fibroblasts produce extracellular matrix components upon wound for self-repair; The hybrid interwoven structure of rigid collagen fiber scaffold and stretchy elastin matrix contributes to not only a nonlinear J-shaped stress-strain mechanoresponsive behavior (i.e., strain stiffening) to avoid tissue damage caused by large deformation while ensuring structural compliance, but also high toughness and fatigue resistance to survive numerous dynamic loadings in daily life. Several effective strategies have been developed to create soft materials that successfully imitate, partly or totally, the ensemble of favorable properties of the skin tissue.

Self-healing elastomers have been realized by incorporating reversible bonds such as hydrogen bonding,[5] metal-ligand coordination,[6] or dynamic covalent bond.[7] However, the inherent weakness of these dynamic interactions imposes a limit to the fracture toughness (fracture energy Γ typically $<100\,\mathrm{J\,m^{-2}}$). To circumvent this limitation, multiple energy dissipation mechanisms collectively toughen the self-healing elastomers, including the introduction of nanocomposite,[8] double networks,[9] supramolecular interactions,[10] and phase separation.[11] Ding et al[12] reported a self-healable elastomer by combining locked-phase, disulfide metathesis and quadruple hydrogen bond into a polyurethane (PU) network to obtain an enhanced toughness (fracture energy of $201.29\,\mathrm{kJ\,m^{-2}}$). While existing toughened elastomers achieved improved fracture toughness,[13] the cyclic fatigue resistance is still highly limited as the fatigue threshold is unaffected by the additional dissipation mechanism off the crack plane, explained by the classic Lake-Thomas model.[14] For instance, natural rubber shows a high fracture toughness of $10\,\mathrm{kJ\,m^{-2}}$, but a low fatigue threshold of $50\,\mathrm{J\,m^{-2}}$.

Introduction of high-energy hard domains into synthetic polymers proved effective to enhance fatigue threshold, such as surface functionalized silica nanoparticles,[15] aligned lamellar MXene structure,[16] and rigid fiber reinforced soft matrix.[17] Lu's group[18] reported a fatigue-resistant polyvinyl alcohol (PVA) hydrogel with preferentially-aligned hier-

---

[*] Prof. X. Jiang,+ Prof. Y. Cheng,+ L. Shi, Prof. J. Sun, Prof. R. Wang
State Key Laboratory of High Performance Ceramics and Superfine Microstructure, Shanghai Institute of Ceramics, Chinese Academy of Sciences
1295 Ding Xi Road, Shanghai 200050, China
E-mail: chengyin@mail.sic.ac.cn
wangranran@mail.sic.ac.cn

Prof. X. Jiang,+ Prof. R. Wang
School of Chemistry and Materials Science, Hangzhou Institute of Advanced Study, University of Chinese Academy of Sciences
Hangzhou 310024, China

Prof. X. Jiang+
Center of Materials Science and Optoelectronics Engineering, University of Chinese Academy of Sciences
1 Sub-lane Xiangshan, Beijing 100049, China

[+] These authors contributed equally to this work.

archical microstructures through a directional freeze-casting method and salting-out process, which exhibited a high fatigue threshold of 300 $J\,m^{-2}$. However, such a strategy is complicated and limited to special material species; Also, the self-healing ability is absent from most of these hard domain toughened elastomers.[11b,15,19] More recently, the skin-inspired hybrid structure has been mimicked to design tough and fatigue-free elastomers.[20] Wu's group[20b] developed a hybrid ionic skin by embedding a self-healable PU framework into a soft hydrogel matrix, to unite self-healing, strain-stiffening, and fatigue-resistance into this water-swollen composite gel. However, the damaged gel required high humidity (RH of 80 %) for effective self-repair due to the water-plasticized mechanism; Also, the structural instability under high temperature and underwater conditions limited its application scenarios. Overall, despite the mentioned advances, it still remains a great challenge to develop a skin-like soft and ionic elastomer that integrates self-healing, high fracture toughness, and fatigue resistance with high environmental robustness.

Herein, by fusing the hierarchical structure of skin tissue and the Bouligand structure in nature, we devised a soft, tough, fatigue-resistant, and self-healable ionic elastomer (STFSI elastomer) through the interlocking of a thermoplastic polyurethane (TPU) fibrous scaffold and an ionic supramolecular biopolymer matrix. The skin-like binary structure endows the STFSI elastomer with a high fracture energy (35.8 $kJ\,m^{-2}$) and fatigue threshold (3479 $J\,m^{-2}$) while maintaining skin-like softness (modulus ~0.7 MPa), stretchability (650 %) and strain-stiffening response (20-fold stiffness enhancement). By engineering the TPU scaffold into a discontinuous Bouligand structure through controllable electrospinning process, the STFSI elastomer is further toughened to exhibit improved toughness (38.7 $MJ\ m^{-3}$), fracture energy (101.6 $kJ\,m^{-2}$), and fatigue threshold (4937 $J\,m^{-2}$), which outpaced most of the reported tough hydrogels and elastomers. Besides, the chemically active and dynamic nature of the supramolecular biopolymer empowers both a highly adhesive interface to various foreign surfaces and a robust self-healing ability (self-healing efficiency of 85 % after 5 min duration). To showcase the versatility and environmental robustness of the STFSI elastomer as structural or sensing elements, we demonstrate its application in a safety cushion with efficient damping and suppressed bouncing, and an underwater robotic sensor with fatigue crack tolerance and immediate self-repairment upon damage.

Results and Discussion

The Design of STFSI Elastomer

Figure 1a illustrates the biomimetic design of the STFSI elastomer. Inspired by the collagen-elastin interlocked binary structure of skin tissue[21] and the Bouligand helicoidal structure of the hyper mineralized natural materials (e.g., hammer-like dactyl clubs of *Odontodactylus scyllarus*[22]), we embedded TPU film prepared by electrospinning into an ionic biopolymer. The binary TPU scaffold-ionic matrix combination resembles the skin-like elastin-collagen assembly. The cross-sectional scanning electron microscope (SEM) reveals a sandwich-like structure of STFSI elastomer, and no visible interlayer delamination or fiber pulling out was observed (Figure S1). The Energy Dispersive Spectrometer (EDS) mapping image also clearly showed the homogeneous distribution of the S element, confirming the successful locking of the ionic biopolymer matrix into the TPU film (Figure S2). Controlled electrospinning humidity allowed a welded interface between adjacent TPU fibers at the contact junctions (Figure S3a), thus enhancing the interfacial strength of the TPU fibers and the overall strength of the TPU film.[23] Adjustable TPU fiber orientation via tuning the electrospinning collection speed was harnessed to construct multilayered TPU fiber stacking with Bouligand structure by imposing an elongation force on the nanofibers to obtain highly aligned fibrous networks under a high electrospinning collection speed of 1000 rpm (Figure S3b-c).

Figure 1b shows the chemical structures of the TPU and the ionic biopolymer. The ionic biopolymer was synthesized by concentration-induced ring-opening polymerization (ROP) of α-lipoic acid (LA) in ethanol (see detailed process in Experimental Section and Figure S4). The as-polymerized polyLA is subject to inverse ring-closing depolymerization and coverts to semicrystalline oligomers within a few minutes, we stabilized the metastable polyLA polymer at room temperature by incorporating 1-ethyl-3-methylimidazolium ethyl sulfate ([EMI][ES]) ionic liquid to form Hydrogen-bonding between carboxyl group of polyLA and [ES], which also acted as a charge transport medium. Furthermore, iron ions were introduced to form metal-ligand coordination to improve mechanical properties. We employed molecular dynamics simulation to construct a unit cell involving polyLA, [EMI][ES] and FeCl3. In this system, the polyLA exhibited a fully flexible chain with typical random coil configuration (Figure 1c). In addition, the stable and homogeneous phase of the ionic biopolymer was further confirmed by the high-resolution AFM phase image (Figure 1d), implying the uniform distribution of iron ion metal clusters. Simultaneously, we also performed molecular dynamics simulation to evaluate the relative interaction energies in the pairs of [EMI] and [ES], polyLA and [EMI], polyLA and [ES], polyLA and iron ions, and polyLA and [EMI][ES] (Figure 1e). The relatively large interaction energies between polyLA and [ES], and polyLA versus iron ions, suggested the thermodynamic stability of COOH···[ES] hydrogen bonding (H-bond) and $COOH\cdots Fe^{3+}$ metal-ligand coordination, which collectively facilitated the polymerization of the meta-stable polyLA into a homogeneous composite ionic biopolymer in the presence of [EMI][ES] and iron ions. We further employed temperature variable FTIR spectroscopy to study the changes of ν(COOH) and ν(S=O) (Figure S5), revealing the changes of COOH···[ES] H-bond and $COOH\cdots Fe^{3+}$ during the heating process, highlighting their roles in stabilizing the ionic biopolymer.

The conductivity of the polymer experienced a decrease and then plateaued as the content of iron ions increased

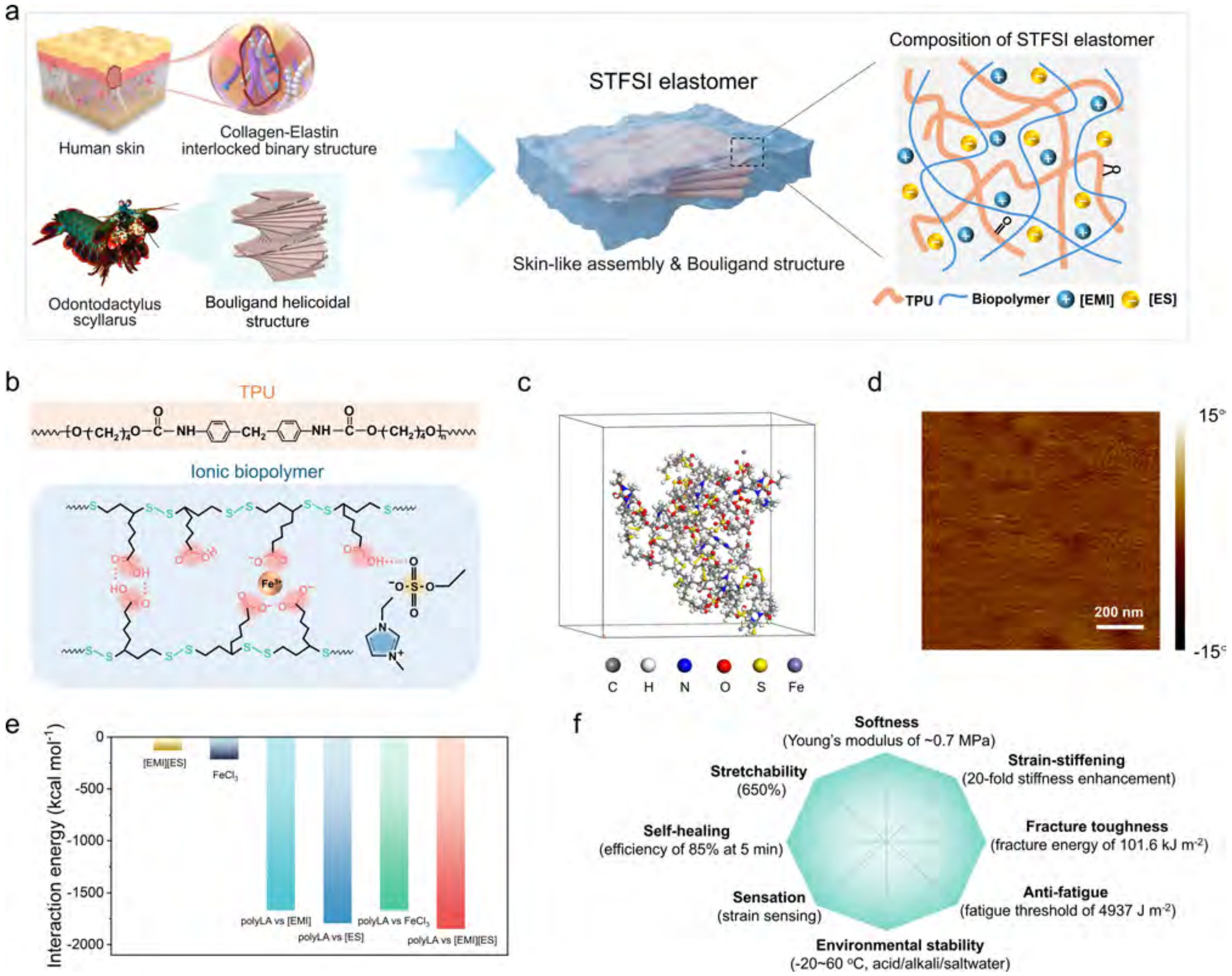

Figure 1. Biomimetic design of the STFSI elastomer. a) The design concept of the STFSI elastomer. Left: collagen-elastin interlocked binary structure of human skin and Bouligand helicoidal structure in the dactyl clubs of Odontodactylus scyllarus; Right: schematic diagram of the composition and structure of STFSI elastomer. b) The chemical structures of the TPU and the ionic biopolymer. c) A simulated polyLA chain with 20 repeating units in the ionic biopolymer. d) Phase AFM image of the transparent ionic biopolymer. Scale bar, 200 nm. e) Interaction energies in six pairs of components by molecular dynamics simulation. f) A summary of STFSI elastomer performance related to structural and sensing use.

(Figure S6a). This could be ascribed to the spatial site-barrier effect induced by the metal-ligand coordination (Fe^{3+}-COOH), which dominates the hindrance to the migration of the cations $[EMI]^+$ (Figure S6). A mass ratio of 1000:1 was determined to obtain an optimized strength, toughness, and conductivity (Figure S7). Moreover, the electrical conductivity of the STFSI elastomer shows an uprising tendency with an elevated temperature due to the enhanced ion migration mobility (Figure S8).

The structural characteristics of ionic biopolymer and STFSI elastomer were characterized by spectroscopic analyses. The amorphous nature of the resultant polyLA ionic gel was confirmed by X-ray diffraction (XRD) characterization (Figure S9), and the successful ROP of LA was evidenced by the splitting of the characteristic Raman peak at 511 cm^{-1} for the disulfide bond into two peaks at 509 cm^{-1} and 524 cm^{-1}, respectively (Figure S10). Fourier Transform Infrared (FT-IR) was used to characterize the functional groups of samples and the interactions between various chemical groups (Figure S11). Such structural synergy and compositional hybridization cooperatively endow the STFSI elastomer with multiple desirable structural/sensing merits (Figure 1f), including mechanical sensation, softness, stretchability, self-healing, strain-adaptive stiffening, anti-fatigue, high fracture toughness, and environmental stability, which mirrors or even surpass the ensemble of peculiar skin tissue properties.

The Strain-stiffening Behavior of the STFSI Elastomer

The mechanical tensile tests were conducted to compare the STFSI elastomer with a single layer randomly aligned TPU film (denoted as STFSI elastomer, unless otherwise specified), a pure TPU film with random alignment, and a pure ionic biopolymer. The recipes of the TPU nanofibrous network and the ionic biopolymer used for preparation of the STFSI elastomer were the same as that of the randomly aligned TPU film and the pure ionic biopolymer for test (experimental details in the Supporting Information). Figure 2a shows that the STFSI elastomer exhibited a pronounced J-shaped true stress-strain curve, similar to that of the pure TPU film but with a larger ultimate tensile strain and strength. The calculated differential modulus shown in Figure 2b confirmed 20 times increase of the stiffness (from 0.45 to 8.9 MPa) of the STFSI elastomer. In contrast, the ionic biopolymer displayed an opposite strain-softening behavior. The strain-adaptive stiffening could be attributed to the orientation, straightening, and stretching of the relatively rigid TPU fibers, corresponding to a load-bearing transfer from the ionic biopolymer to the TPU film (Figure S12). In addition, unlike previously reported supramolecular elastomers, the STFSI elastomer possessed a strain rate-insensitive stiffening (Figure S13), which resembles human skin more precisely[24] and verifies the dominating role of the TPU film in governing the stiffening response. To demonstrate the protection by strain-stiffening, we applied increasing loads on a strip of the STFSI elastomer (Figure 2c). A small load of 100 g led to immediately a long elongation (65 %) of the strip; further increasing the load to 400 g, the increased elongations were obviously suppressed, preventing the sample damage caused by overstretch.

A continuous loading-unloading test with increasing strains (from 10 % to 500 %) was implemented to the STFSI elastomer to calculate the corresponding dissipation energy

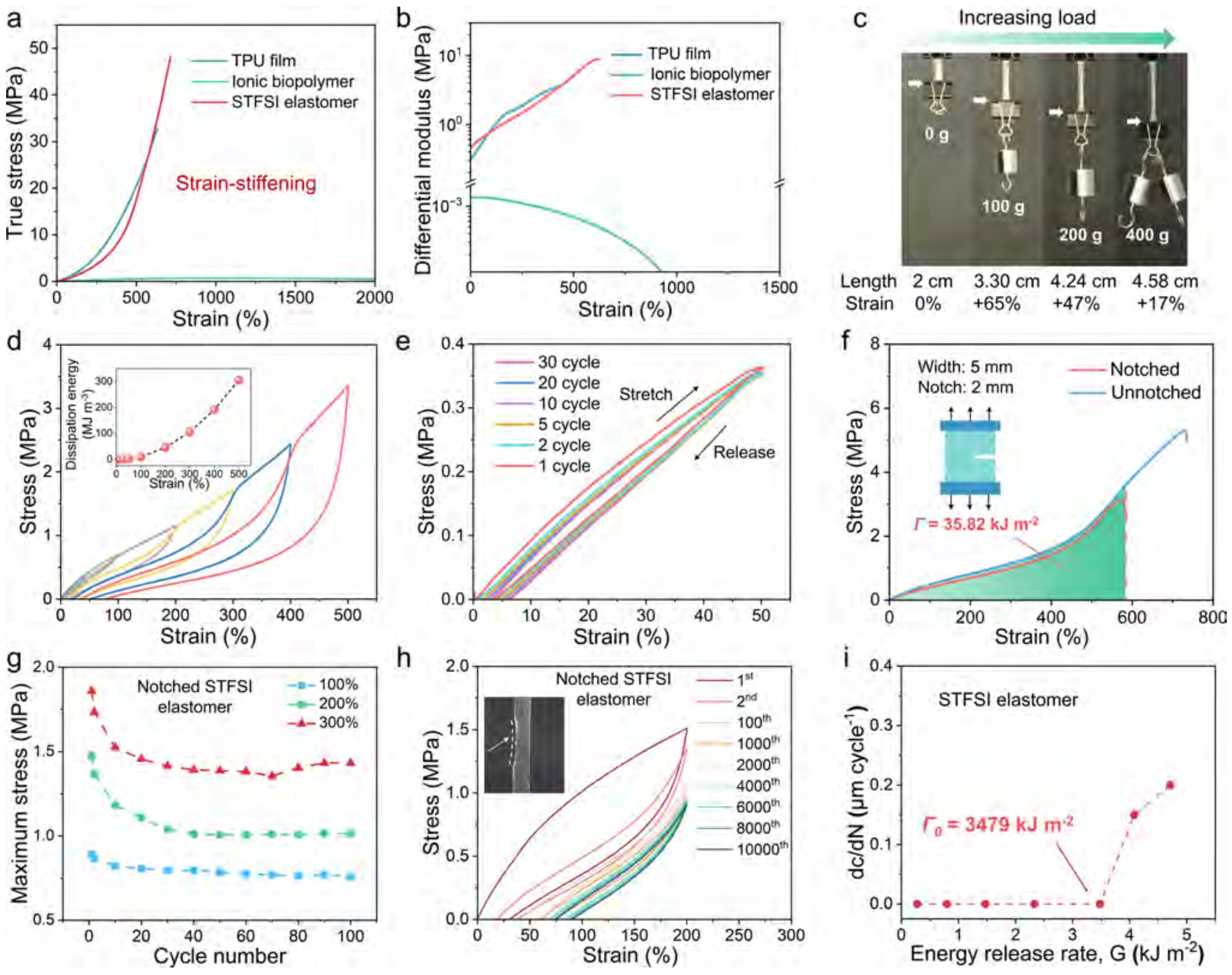

Figure 2. Mechanical properties of the random STFSI elastomer. a) True stress-strain curves of the STFSI elastomer, pure TPU film, and the ionic biopolymer and b) corresponding differential modulus curves. c) Strain-stiffening protection demonstration of the STFSI elastomer (sample size: 20×5 ×0.2 mm^3). d) Tensile loading – unloading curves at different strains (10 %, 30 %, 50 %, 100 %, 200 %, 300 %, 400 %, 500 %) of STFSI elastomer. The inset shows the dissipation energy at each loading – unloading cycle. e) Tensile stretch-release cycles at a strain of 50 % with no resting time. f) Typical stress-strain curves of the unnotched and notched STFSI elastomer. g) The maximum stress of the notched STFSI elastomer during the cyclic stretching-releasing. (applied strain at 100 %, 200 % and 300 %). h) Tensile stretch-release cycles of notched STFSI at 200 % strain (inset: crack passivation of notched STFSI during cyclic tensile test. i) Crack growth per cycle, *dc/dN*, measured at various amplitudes of energy release rate G for STFSI elastomer. By definition, the fatigue threshold Γ_0 is equal to the critical energy release rate.

(Figure 2d). The residual strain under 100 % strain was minimal (2.8 % for 50 % test strain and 6.9 % for 100 % test strain), and the dissipation energy rose sharply when the stretch strain surpassed 100 % strain, indicating that the STFSI elastomer is highly elastic within small strain range and enormously dissipative at large deformation. Furthermore, successive stretch-release cycles at a strain of 50 % exhibited that, after the first several cycles, the stretch-release curves stayed almost overlapped, verifying a stable mechanical response during cyclic loadings (Figure 2e).

Fracture Toughness and Fatigue Resistance of the STFSI Elastomer

To determine the fracture toughness of the STFSI elastomer, the single-notch method was adopted to subject the sample with a precut crack to a monotonic load. The exceptional crack resistance during the tearing process was illustrated in the stress-strain response of the notched STFSI elastomer sample (Figure 2f), giving a fracture energy of 35.82 $\mathrm{kJ\,m^{-2}}$, much higher than that observed in the pure TPU film (18.39 $\mathrm{kJ\,m^{-2}}$) and the ionic biopolymer (1.46 $\mathrm{kJ\,m^{-2}}$) (Figure S14). The markedly enhanced fracture toughness of the STFSI elastomer stemmed from the extra mechanical dissipation in the dissipation zone around the crack tip provided by the ionic biopolymer matrix, such as the ionic polymer short-chain breakage, viscoelastic dissipation and hydrogen bonding breakage. During cyclic stretching-releasing of the notched STFSI elastomer (applied strain of up to 300 %), most of the energy dissipation and strength softening occurred within the initial several loading cycles (Figure 2g and Figure S15), and no crack propagation and strength attenuation were observed during the subsequent loading cycles.

The fatigue fracture threshold of a material is defined as the energy required to fracture a single layer of polymer chains, showing the resistance to fatigue crack propagation after prolonged loading cycles. To measure the fatigue threshold of the STFSI elastomer, we performed cyclic tensile tests to a notch sample (Figure 2h). The STFSI elastomer revealed a high fatigue threshold of 3479 $\mathrm{J\,m^{-2}}$, which was 37 times higher than that of the ionic biopolymer (94 $\mathrm{J\,m^{-2}}$) (Figure S16). For the STFSI elastomer, the high-energy TPU fibers significantly increased the fracture energy per unit area, resulting in a considerably improved fatigue resistance. Note that, most toughened elastomers have high fracture toughness but are highly fatigue-prone with a low fatigue threshold. Apparently, our STFSI elastomer exhibited both high fracture energy and fatigue threshold.

In situ SEM Tensile Test and Simulation Analysis of the High Fracture Toughness

To understand the underlying mechanism of enhanced fracture toughness, we recorded the evolution of the crack propagation in notched samples of the STFSI elastomer and the ionic biopolymer (Figure 3a and 3b) via the in situ SEM tensile test. For the STFSI elastomer, the notch opened up and turned blunt firstly owing to the high softness of the ionic biopolymer (low elastic modulus of 0.17 MPa). Then, crack deflection and fiber bridging occurred as the crack further advanced, which alleviated the stress concentration and pinned the crack at the high-energy TPU fiber zones to impede the crack propagation. The STFSI elastomer did not fracture even at the maximum displacement during the in situ tensile test (gauge length of 10 mm, maximum displacement of 10 mm). As a comparison, the ionic biopolymer went through a crack blunting under low extension (displacement of 6 mm), followed by a fast crack propagation till complete rupture at displacement of 8.5 mm. Figure 3c summarized the distinct crack propagation behaviors of the STFSI elastomer and the ionic biopolymer. The in situ SEM characterization clearly evidenced the crack pinning effect of the high-energy TPU scaffold for enhanced fracture toughness. Additionally, macro-photography was adopted to capture the strained and recovered states, clearly revealing a progressive crack deflection for the STFSI elastomer, and a forward-way (along the pre-cut direction) crack propagation for the ionic biopolymer (Figure S17).

Furthermore, finite element analysis (FEA) was performed using ABAQUS software to assess the FEA models and corresponding Von Mises Stress distribution of the ionic biopolymer (Figure 3d) and the STFSI elastomer (Figure 3e). Under tensile loading, the ionic biopolymer exhibited an obvious stress concentration at the crack tip, accounting for the rapid crack propagation. For comparison, stress concentration was efficiently transferred to the interconnected TPU scaffold in the STFSI elastomer due to the high modulus ratio of TPU fiber to the ionic biopolymer (stiffness ratio of 7), and the high interfacial strength between the scaffold and the matrix. As a result, the crack deflection and fiber bridging both contributed to the resistance to crack propagation.

Bouligand Structure Toughened STFSI Elastomer

Bouligand structure with rotated nanofiber arrangements is widely present in many biological materials such as fish scale and lobster underbelly. It is proved efficient to toughen materials due to the energy dissipation by the rotating anisotropic layers.[25] The orientation of the TPU fibers could be programmed by a developed layer-by-layer electrospinning method (Figure 4a) to obtain TPU nanofibrous membranes stacked with various rotation angles as confirmed by the SEM characterization (Figure S18). To verify the assembly controllability and explore the structure-performance relationship, we fabricated STFSI elastomers with a single unidirectional TPU layer (defined as unidirectional STFSI elastomer), and multiple TPU layers of periodical rotation angles including 0°, 20°, 45°, and 90° (defined as 0° rotated STFSI elastomer, et al.).

To begin with, we performed single-notch tensile test to the unidirectional STFSI elastomer in a parallel or vertical stretching manner. The mechanical responses were highly related to the stretching direction as seen in Figure 4b. The

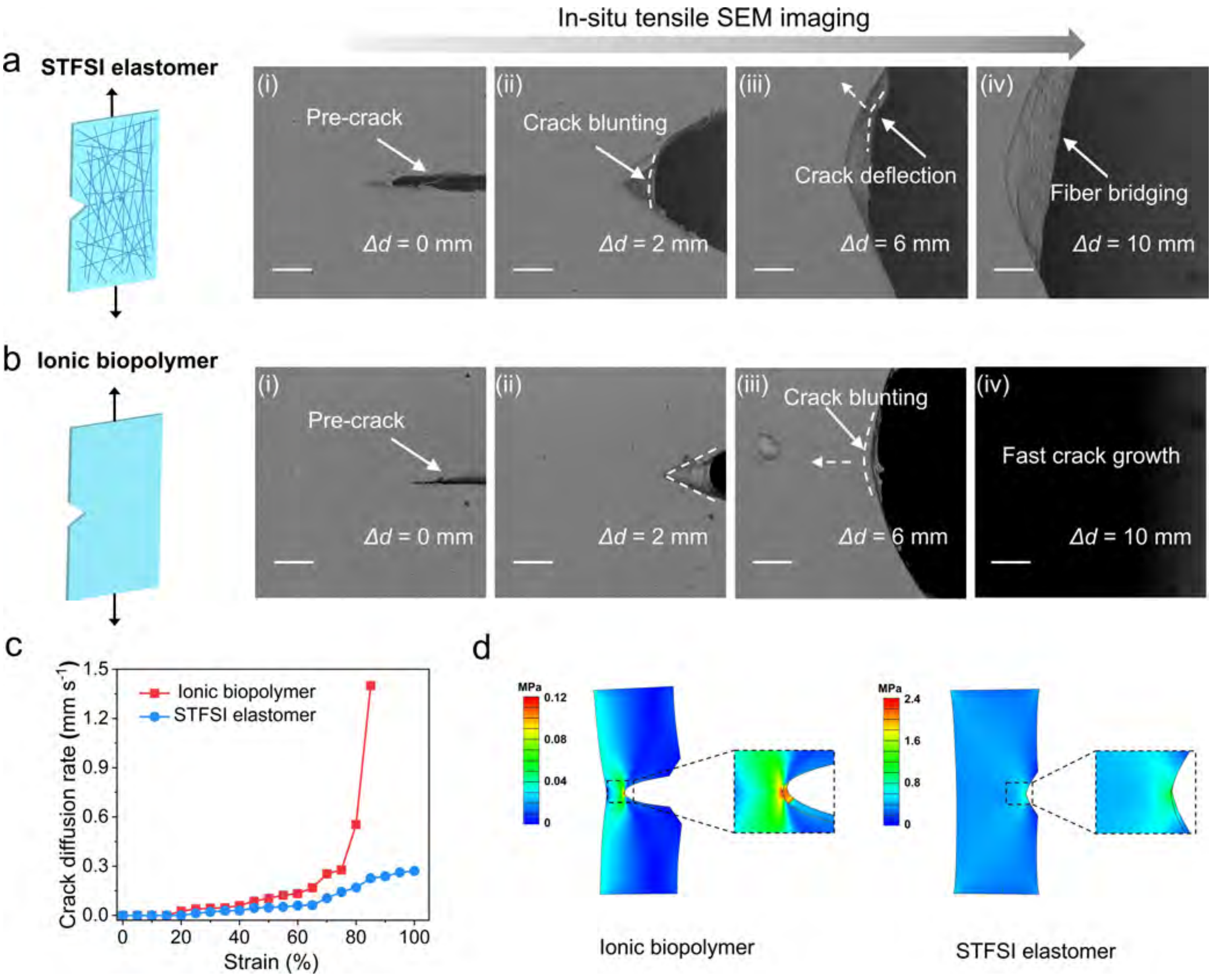

Figure 3. Toughening mechanism analysis of the STFSI elastomer. In situ SEM tensile test observation of pre-cracked specimens of the STFSI elastomer (a) and the biopolymer (b). The white dotted arrows represent the direction of crack propagation, scale bar: 300 μm. c) Crack diffusion rates of the STFSI elastomer and the ionic elastomer during in situ SEM tensile test. d) The stress nephograms of the ionic biopolymer and the STFSI elastomer during stretching (applied strain of 80 %).

unidirectional STFSI elastomer exhibited much higher tensile strength (7.3 MPa) and fracture energy (74.3 $\mathrm{kJ\,m^{-2}}$) in parallel than those of vertical stretching (Figure 4c), which could be attributed to the ready fiber bridging of the TPU fibers aligned with the stretching direction. Cyclic tensile tests further confirmed a fatigue threshold of 1442 $\mathrm{J\,m^{-2}}$ for the parallel stretching direction (Figure 4d), lower than that of the STFSI elastomer with a single layer randomly aligned TPU film (3479 $\mathrm{J\,m^{-2}}$), implying the beneficial effect of multi-directional alignment of TPU fibers to fatigue resistance.

Furthermore, tensile tests were conducted to STFSI elastomers with Bouligand structure of different deviation angles, and a STFSI elastomer with multilayered randomly aligned TPU film (Figure 4e). The 20° rotated STFSI elastomer exhibited an optimal toughness of 38.7 $\mathrm{MJ\ m^{-3}}$ (Figure 4f), outperforming the randomly aligned and other rotation angle counterparts. Monotonic tensile tests to notched samples revealed a highest fracture energy (101.6 $\mathrm{kJ\,m^{-2}}$) of the 20° rotated STFSI elastomer (Figure 4g). To understand the rotation angle-dependent mechanical performance, we conducted in situ tensile SEM imaging of the notched STFSI elastomers with varying rotation angles (from 0° to 90°), and SEM observation of the crack front geometry of the corresponding fractured samples. Crack blunting emerged in all the tested samples due to the high fiber/matrix modulus ration (shown in Figure S19), implying extensive load transfer and energy dissipation. The increase of rotation angle led to weakened elastic modulus and strength, mainly brought about by decreased contribution of the TPU fibers in uniaxial load bearing.[26] The crack front geometry (shown in Figure 4h) revealed significant interlayer slipping for the samples with deviated angles from the uniaxial loading direction (20°, 45°

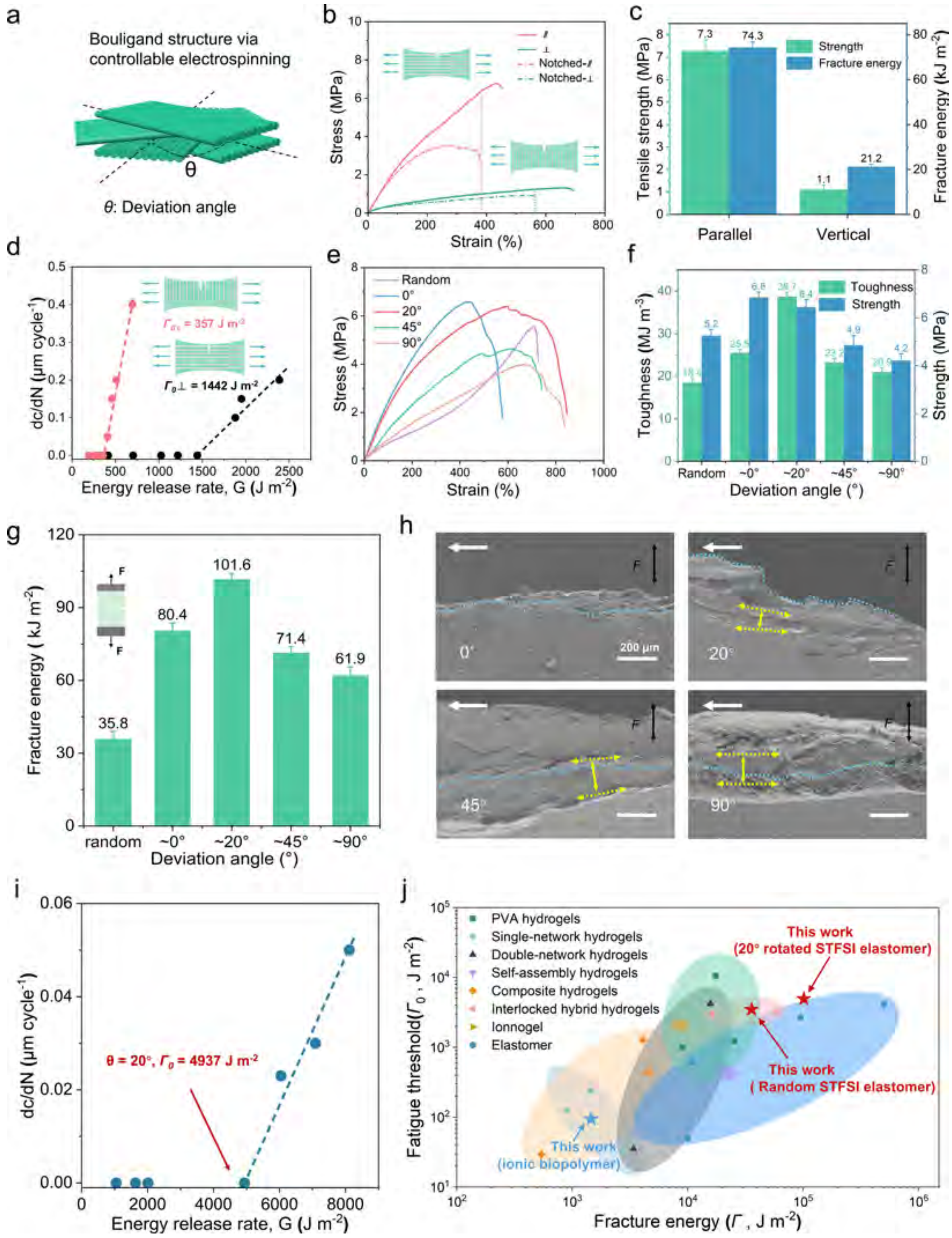

Figure 4. Bouligand structure toughened STFSI elastomer. a) Schematic diagram of Bouligand structure at different rotation angles ($\theta = 0°$, 20°, 45°, and 90°). b) The tensile stress-strain curves of notched and unnotched unidirectional STFSI elastomers in a parallel or vertical stretching manner. c) Tensile strength and fracture energy of unidirectional STFSI elastomer in a parallel or vertical stretching manner. d) Crack growth per cycle, dc/d*N*, measured at various amplitudes energy release rate G for unidirectional STFSI elastomer in a parallel or vertical stretching manner. e) Tensile stress-strain curves of STFSI elastomers with Bouligand structure of different deviation angles, and a STFSI elastomer with multilayered randomly aligned TPU film. f) Tensile strength and toughness at different deviation angles. g) Tested fracture energy at different deviation angles. h) SEM images of the crack front geometry of fractured STFSI elastomers of various rotation angles. White arrows indicate the direction of pre-crack, yellow arrows indicate interlayer slipping of TPU membranes, blue dotted lines indicate the crack propagation path. Scale bar: 200 μm. i) Crack growth per cycle, dc/dN, measured at various amplitudes of energy release rate G for the notched 20° rotated STFSI elastomer. j) Fatigue threshold (Γ_0) and fracture energy (Γ) of the randomly aligned STFSI elastomer, the 20° rotated STFSI elastomer, and previously reported toughened hydrogels and elastomers.

and 90° rotated samples). Such interlayer slipping dissipation allowed a comparable toughness of the 45° and 90° rotated STFSI to that of the 0° rotated STFSI. For the 20° rotated STFSI elastomer, the crack front geometry not only revealed an interlayer-slipping, but also a marked twisting of crack propagation path. The twisted crack propagation gave rise to an amplified geodesic crack front length, leading to geometric toughening to enable an optimized tougness and fracture energy.[27]

Similarly, cyclic tensile test to the notched 20° rotated STFSI elastomer confirmed a super-high fatigue threshold (4937 $\mathrm{J\,m^{-2}}$) (Figure 4h). We compared the mechanical performance of our STFSI elastomers with other reported tough elastomers and hydrogels, in terms of fracture toughness and fatigue resistance. The randomly aligned STFSI elastomer and the 20° rotated STFSI elastomer rank in the top class among various toughened hydrogels and elastomers, such as PVA hydrogels, double-network hydrogels, composite hydrogels, and tough elastomers (Figure 4i and Table S1).

Self-adhesive, Self-healing, and Environment-tolerant Properties

The ionic biopolymer matrix possesses abundant functional groups including polar carboxy group and metal ions, collectively leading to strong interfacial interaction with various substrates, such as hydrogen bonding and metal-ligand coordination (Figure 5a). In addition, the dynamic chains of the ionic biopolymer may penetrate the micropores of substrate surfaces to form mechanically interlocked adhesion enhancement. Using a probe tack adhesion test, the STFSI elastomer exhibited strong adhesion to various common substrates, including wood, glass, copper, and PTFE (Figure 5b). Besides, for the adhesion to porcine skin, the STFSI elastomer displayed a higher adhesive strength of 170 kPa than that of the pure ionic biopolymer and other commercial tapes (Figure 5c), indicating a reliable adhesion to skin for wearable sensing applications. Compared with the ionic biopolymer, the adhesion enhancement of the STFSI elastomer is derived from the deformation of the TPU fibrous network near the interface and the facilitated stress transfer from the interface into the soft matrix by the TPU fibers to induce extended mechanical dissipation.

The rich dynamic interactions at the surface of the ionic biopolymer drives us to leverage the strong cohesive strength to autonomously heal damaged STFSI elastomers. Figure 5d shows a “bridging” strategy: two pieces of completely severed STFSI elastomer strip were aligned to overlap near the cutline and pressed with a 10 N weight for varying durations. The bridging-assisted overlap area affects the self-healing performance: larger overlap region gave a higher healing efficiency as confirmed by experiments of varying overlap areas (Figure S20). In an ambient environment (20 °C in the air), we conducted the “bridging” assisted experiments with varying self-healing durations of 30s, 2 min, 5 min, and 30 min (Figure 5f). Longer self-healing durations enabled higher mechanical performance. For instance, a 5 min duration caused a maximum elongation strain of 575 %, corresponding to a self-healing efficiency η

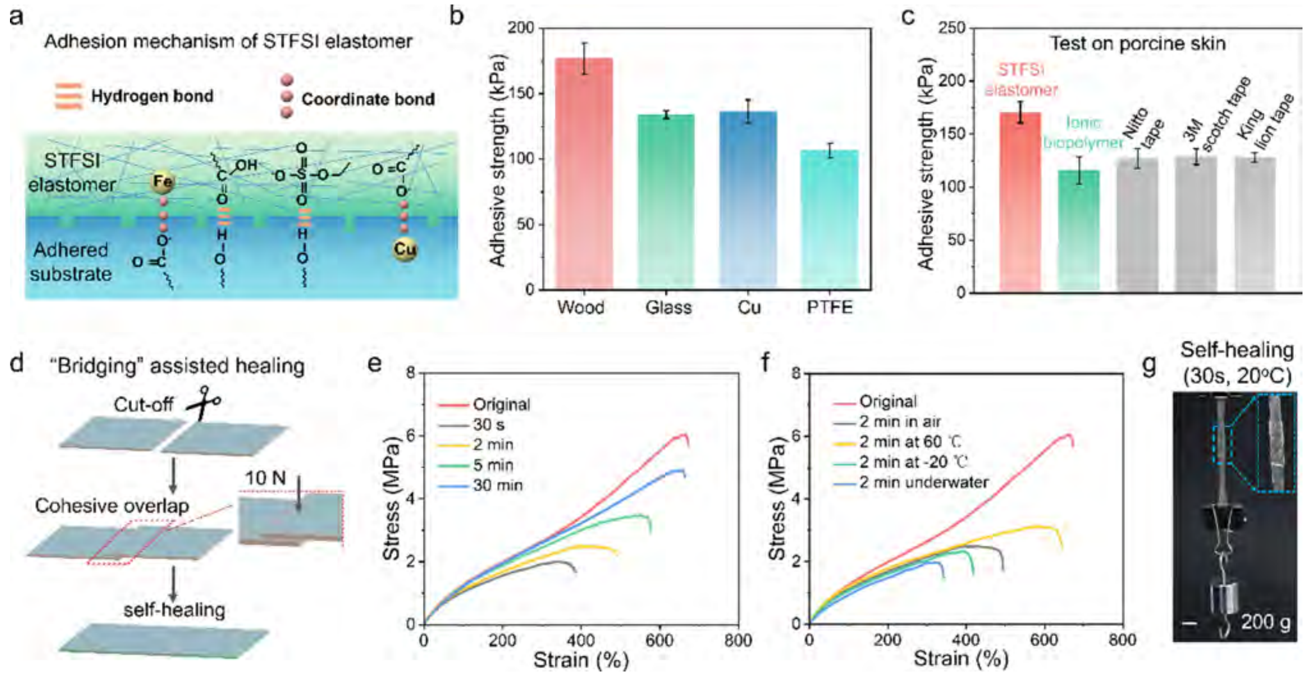

Figure 5. Self-adhesive and self-healing properties of STFSI elastomer. a) Schematic illustration of adhesion mechanism between STFSI elastomer and various types of substrates. b) Adhesion strength of STFSI elastomer on various types of substrates using a probe tack adhesion test. c) Comparison of adhesion strength on porcine skin of STFSI elastomer, ionic biopolymer and other. commercial tapes (three kinds of tapes from brands of Nitto, 3 M, and King). d) Schematic diagram of “bridging” assisted self-healing strategy. e) The tensile stress-strain curves of the original and self-healed STFSI elastomer with varying healing durations. f) The tensile stress-strain curves of the original and self-healed STFSI elastomer under different extreme conditions. g) Photograph of self-healed STFSI elastomer withstand a weight of 200 g after a quick 30 s healing at 20 °C in the air. Adhesion area: 5 mm ×10 mm.

of 85 % in terms of the recovered fracture strain. The self-healing efficiencies for other durations were 57 % (30s), 73 % (2 min), and 98 % (30 min) respectively. Furthermore, the self-healing under extreme conditions were tested (Figure 5e), including 2 min duration at high (60 °C) and low (−20 °C) temperatures in the air, and underwater (20 °C). Compared with the 2 min healing in the air (η of 80 %), the STFSI elastomer obtained self-healing efficiency of 89 % and 35 % at 60 °C and −20 °C respectively, owing to the temperature-sensitive chain mobility and dynamic interactions. For the underwater healing (the whole process of cutting and healing was kept underwater), the self-healing efficiency decreased to 32 % probably due to the moisture trapped at the healing interface. Figure 5g demonstrates that a self-healed STFSI elastomer could withstand a weight of 200 g after a quick 30s healing at 20 °C in the air.

Besides the underwater and varied temperature range conditions, we also tested and compare the mechanical properties before and after treatment under extreme conditions (Experimental Section). The STFSI elastomer were soaked in high-concentrated saltwater, strong acid and alkali, and no obvious mechanical degradation were observed after the harsh tests, verifying the robust environmental stability for practical outdoor use (Figure S21).

Strain Sensing Properties of the STFSI Elastomer

The strain-sensing properties of the STFSI elastomer were systematically investigated. The sensitivity is assessed using gauge factor (GF, relative change in resistance per unit strain), represented by the slope of the curve. Figure 6a shows the relative resistance change of the STFSI elastomer upon the applied strain, and the GF were 1.37 and 2.54 at low (0–150 %) and large (150 %–300 %) strain ranges, respectively. Figure 6b records the resistance change upon a quasi-transient strain input of 5 %, and the response time and recovery time were measured to be 224 ms and 249 ms.

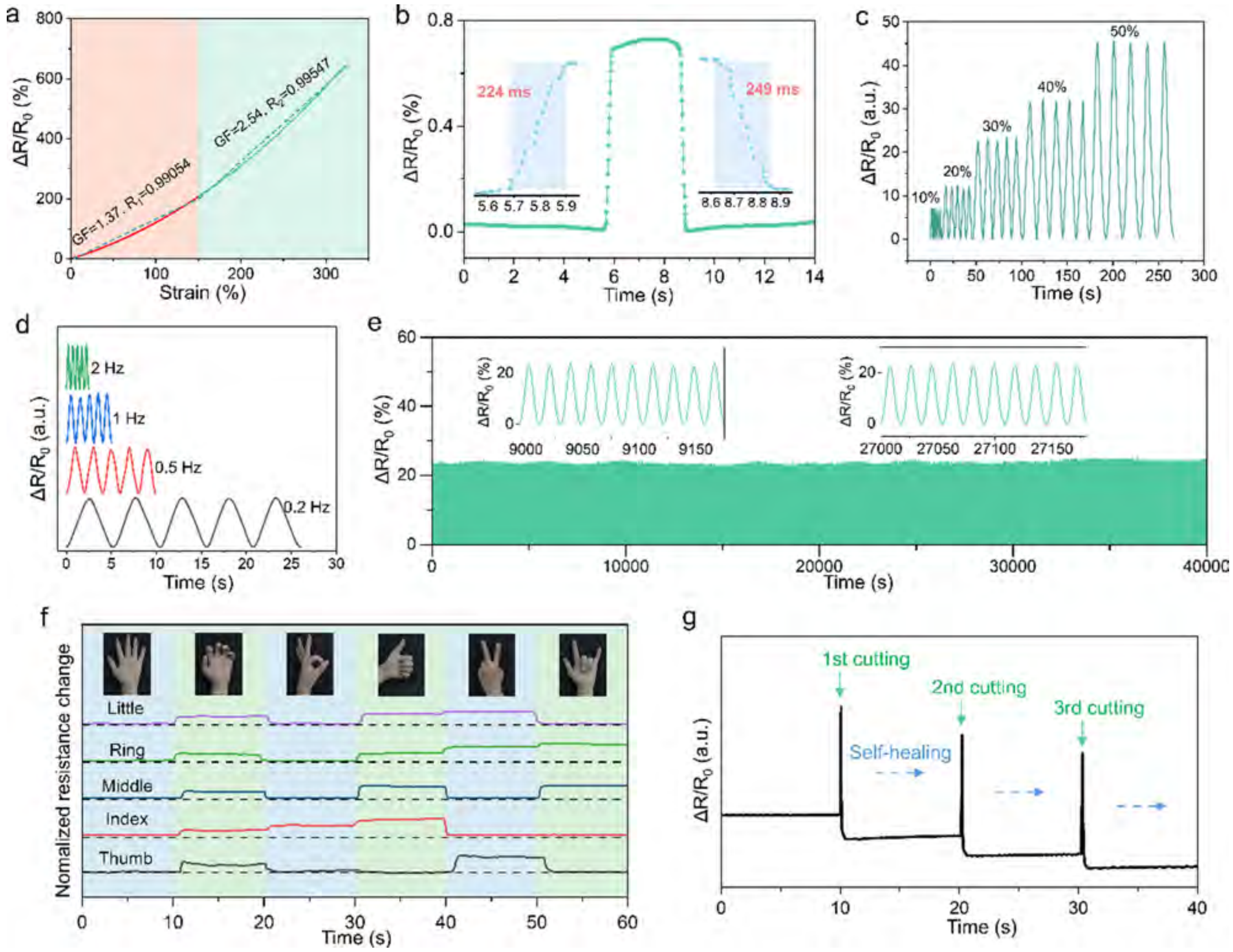

Figure 6. Strain sensing properties of the STFSI elastomer. a) The relative resistance changes of STFSI elastomer with gauge factors marked at different strains. b) Response and recovery time of STFSI elastomer. c) Relative resistance variation of STFSI elastomer under cyclic stretching from 10% to 50% d) Relative resistance variation of STFSI elastomer under strain of 30% at various frequencies from 0.2 to 2 Hz. e) The long-term strain sensing durability of STFSI elastomer during 2500 cycles of 30% strain stretch-release. f) Gesture identification through combination of 5 STFSI elastomer sensors adhered to fingers. g) Relative resistance change of the STFSI elastomer sensor during 3 cutting-and-healing events.

Cyclically stretching at fixed strains ranging from 10 % to 50 % resulted in stable and repeatable electrical responses, indicating the sensing signal reproducibility (Figure 6c). Moreover, the STFSI elastomer could respond to strain stimuli (30 %) with a wide frequency range from 0.2 to 2 Hz (Figure 6d). A 2500 cyclic stretch test at strain of 30 % confirmed high durability and signal stability (Figure 6e). The self-adhesive capability allowed the STFSI elastomers to be readily attached to fingers with no external aid and served as motion detectors of finger bending. Different hand gestures could be distinguished through the distinct sets of electrical responses (Figure 6f). Interestingly, the STIFS elastomer could immediately regain electrical conductivity after "bridging" assisted self-healing for multiple cutting-off events, accompanied by an electric resistance decrease of the STFSI elastomer with a shortened length governed by the law of resistance (Figure 6g). The fast self-healing allows the STIFS elastomer to survive accidental damages as robust strain sensors.

Safety Cushion and Robotic Sensor Applications

Ideal safety cushion for falling objects requires high damping and suppressed rebounding to ensure a safe landing. The verified high toughness and efficient mechanical energy dissipation of the STFSI elastomer encourages its exploitation in construction of high-quality safe cushion. Figure 7a depicts the testing method for performance evaluation: an iron ball of 50 g fell from a certain height *h*, and landed to the safety cushion with a buffering distance *d* and rebounding height *r*. The buffering ratio (defined as *d/h*) and rebounding ratio (defined as *r/h*) were recorded at different falling heights for safety cushions made from a randomly

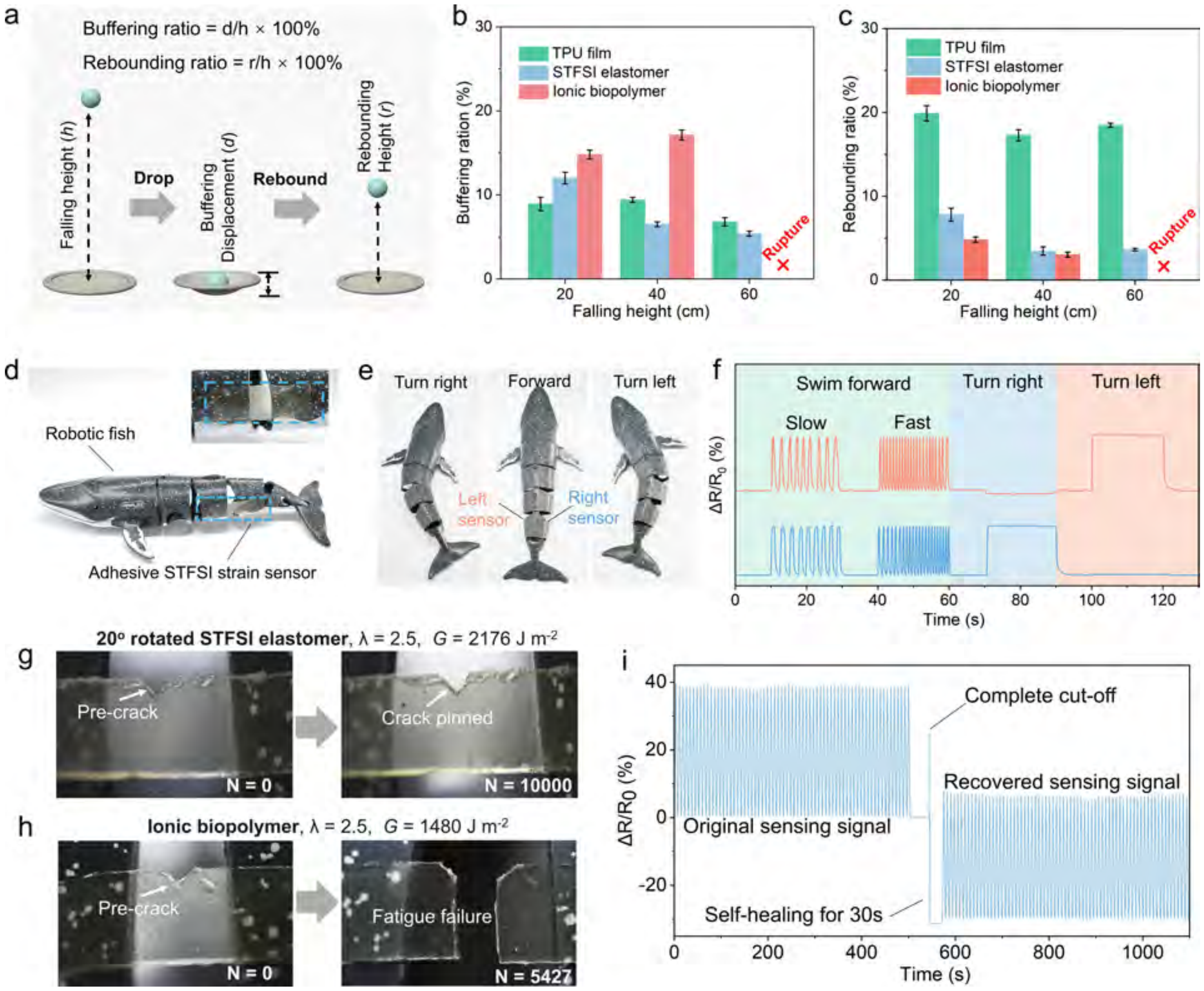

Figure 7. STFSI elastomer based safety cushion and robotic sensor. a) Schematic diagram of the falling ball experiment. b) Buffering ratio and c) rebounding ratio of the iron ball falling onto a randomly aligned TPU film, an ionic biopolymer, and a 20° rotated STFSI elastomer with Bouligand structure. d) Digital photographs of the STFSI elastomer sensors attached to the two sides of a shakeable tail of a fish-like robot. e) Digital photographs of the tail states under different motion modes. f) Signal response under different motion modes. g) Fatigue test to a pre-cracked 20° rotated STFSI elastomer (stretch of 2.5, corresponding to an energy release rate of 2176 J m^{-2}). No crack propagation after 10,000 cycles. h) Fatigue test to a pre-cracked ionic biopolymer (stretch of 2.5, corresponding to an energy release rate of 1480 J m^{-2}). Fatigue at 5427 cycles. i) Signal response of STFSI elastomer sensor during a complete cut-off and 30 s self-healing.

aligned TPU film, an ionic biopolymer, and a 20° rotated STFSI elastomer with Bouligand structure. The TPU film and the STFSI elastomer provided buffering ratios of the same level, whereas the ionic biopolymer had larger buffering ratios due to its high softness (Figure 7b). Unfortunately, the ionic biopolymer ruptured when falling height increased, limited by the low impact toughness. The STFSI elastomer displayed much lower rebounding ratios than that of the TPU film (Figure 7c), owing to its high energy dissipation ability. The 20° rotated STFSI elastomer with softness, impact resistance and energy absorption capacity are particularly suitable for high-quality damping and protection.

Two strips of 20° rotated STFSI elastomers were directly attached to the two sides of a shakable tail of a fish-like robot with the aid of the selff-adhesiveness (Figure 7d). When the robot fish swam forward, the tail whipped left and right continuously; For turning right or left, the tail kept bending to the right or left (Figure 7e). The STFSI elastomer-based strain sensors could produce distinct response signals to capture different swimming states, such as swimming forward slow and fast, turning right or left (Figure 7f). To assess the fatigue resistance, a 20° rotated STFSI elastomer with a precut crack (~1/5 of the overall width) was utilized as a strain sensor for the robotic fish. The notched sensor could sustain 10,000 cycles of tail whipping at an energy release rate of $2176\,\mathrm{J\,m^{-2}}$ (applied strain of 150 %) without any observable crack propagation (Figure 7g). As a comparison, a notched sensor based on the ionic biopolymer experienced a crack propagation and complete fracture failure after 5427 cycles of tail whipping at an energy release rate of $1480\,\mathrm{J\,m^{-2}}$ (applied strain of 150 %) (Figure 7h). Moreover, after a catastrophic cutting-off damage, the STFSI elastomer sensor recovered the sensing functionality immediately after a "bridging" assisted self-healing within 30 s (Figure 7i). The sensing performance of the STFSI strain sensor under high (60 °C and low (−20 °C) temperatures was also confirmed by stable output signals (Figure S22). Equipped with the superb fatigue resistance, self-healing capacities and environmental stability, the STFSI elastomer enables robust robotic sensing to survive accidental impacts in practical outdoor applications.

Conclusion

In this work, we developed a soft and tough elastomer (STFSI elastomer) combining the skin-like binary assembly and Bouligand structure by infiltration of a supramolecular ionic biopolymer into an electrospun TPU fibrous scaffold. This distinctive skin-like assembly allows efficient stress transfer from a soft dissipative matrix to a rigid scaffold during stretching, leading to strain-adaptive stiffening, high fracture toughness and fatigue resistance. The STFSI elastomer with Bouligand structure of helicoidal TPU layer alignments achieves optimized mechanical toughness owing to interlayer slipping dissipation and twisted crack propagation. Bouligand structure for mechanical toughening are mostly based on stiff and inorganic materials for both mineralized natural structures and previously reported biomimetic counterparts,[25a,28] due to the complexity in manipulating soft/stretchable fibrous networks into highly aligned and orientation controllable configurations. We here developed a scalable electrospinning-based integration of soft Bouligand structure and skin-like assembly. In addition, the choice of the ionic biopolymer as the matrix further confers skin-like combinatory properties of self-healing, self-adhesion and mechano-sensing. This rational structural/compositional hybridized design provides a new route to mechanically soft, tough and sensitive materials for multi-functional applications. The versatility for structural and sensing applications have been well evidenced by a safe cushion with efficient damping and suppressed rebounding, and a robotic sensor with excellent fatigue crack tolerance and instant self-repair upon catastrophic damage.

Supporting Information

Supporting Information is available containing experimental methods and supporting Figures that support the main discussion of the article.

Acknowledgements

This work was financially supported by the National Natural Science Foundation of China (Grant No 62122080, 6226113655, 52203365), the Natural Science Foundation of Shanghai (22ZR1481700, 22dz1205000), Shanghai Science and Technology Commission Project-International Science & Technology Cooperation Program (23520711000).

Conflict of Interest

The authors declare no conflict of interest.

Data Availability Statement

The data that support the findings of this study are available from the corresponding author upon reasonable request.

Keywords: biomimetic design · soft ionic elastomer · self-healable · fatigue-free · environment-tolerant

---

[1] a) Y. Hao, Q. Yan, H. Liu, X. He, P. Zhang, X. Qin, R. Wang, J. Sun, L. Wang, Y. Cheng, *Adv. Funct. Mater.* **2023**, *33*, 2303881; b) Z. Sun, Z. Zhang, C. Lee, *Nat. Electron.* **2023**, *6*, 941–942.

[2] A. Chortos, J. Liu, Z. Bao, *Nat. Mater.* **2016**, *15*, 937–950.

[3] D. Won, J. Bang, S. H. Choi, K. R. Pyun, S. Jeong, Y. Lee, S. H. Ko, *Chem. Rev.* **2023**, *123*, 9982–10078.

[4] a) Y. Cheng, Y. Zhou, R. Wang, K. H. Chan, Y. Liu, T. Ding, X.-Q. Wang, T. Li, G. W. Ho, *ACS Nano* **2022**, *16*, 18608–18620; b) X. Zhao, X. Chen, H. Yuk, S. Lin, X. Liu, G. Parada, *Chem. Rev.* **2021**, *121*, 4309–4372.

[5] A. Pena-Francesch, H. Jung, M. C. Demirel, M. Sitti, *Nat. Mater.* **2020**, *19*, 1230–1235.
[6] Y. Cheng, K. H. Chan, X.-Q. Wang, T. Ding, T. Li, C. Zhang, W. Lu, Y. Zhou, G. W. Ho, *Adv. Funct. Mater.* **2021**, *31*, 2101825.
[7] Z. Zou, C. Zhu, Y. Li, X. Lei, W. Zhang, J. Xiao, *Sci. Adv.* **2018**, *4*, eaaq0508.
[8] Y. Wang, R. Shu, X. Zhang, *Angew. Chem. Int. Ed.* **2023**, *62*, e202303446.
[9] T. Matsuda, T. Nakajima, J. P. Gong, *Chem. Mater.* **2019**, *31*, 3766–3776.
[10] J. Kang, D. Son, G.-J. N. Wang, Y. Liu, J. Lopez, Y. Kim, J. Y. Oh, T. Katsumata, J. Mun, Y. Lee, L. Jin, J. B. H. Tok, Z. Bao, *Adv. Mater.* **2018**, *30*, 1706846.
[11] a) H. Lei, L. Dong, Y. Li, J. Zhang, H. Chen, J. Wu, Y. Zhang, Q. Fan, B. Xue, M. Qin, B. Chen, Y. Cao, W. Wang, *Nat. Commun.* **2020**, *11*, 4032; b) X. Liang, G. Chen, S. Lin, J. Zhang, L. Wang, P. Zhang, Z. Wang, Z. Wang, Y. Lan, Q. Ge, J. Liu, *Adv. Mater.* **2021**, *33*, 2102011; c) Y. Chen, A. M. Kushner, G. A. Williams, Z. Guan, *Nat. Chem.* **2012**, *4*, 467–472; d) M. Wang, P. Zhang, M. Shamsi, J. L. Thelen, W. Qian, V. K. Truong, J. Ma, J. Hu, M. D. Dickey, *Nat. Mater.* **2022**, *21*, 359–365.
[12] J. Chen, Y. Gao, L. Shi, W. Yu, Z. Sun, Y. Zhou, S. Liu, H. Mao, D. Zhang, T. Lu, Q. Chen, D. Yu, S. Ding, *Nat. Commun.* **2022**, *13*, 4868.
[13] a) G. J. Lake, P. B. Lindley, *J. Appl. Polym. Sci.* **1964**, *8*, 707–721; b) A. N. Gent, P. B. Lindley, A. G. Thomas, *J. Appl. Polym. Sci.* **1964**, *8*, 455–466.
[14] G. J. Lake, A. G. Thomas, D. Tabor, *Proc. R. Soc. Lond. A* **1967**, *300*, 108–119.
[15] J. Steck, J. Kim, Y. Kutsovsky, Z. Suo, *Nature* **2023**, *624*, 303–308.
[16] J. Xu, Y. Li, T. Liu, D. Wang, F. Sun, P. Hu, L. Wang, J. Chen, X. Wang, B. Yao, J. Fu, *Adv. Mater.* **2023**, *35*, 2300937.
[17] J. Huang, A. Chen, S. Han, Q. Wu, J. Zhu, J. Zhang, Y. Chen, J. Liu, L. Guan, *Adv. Sci.* **2023**, *10*, 2301116.
[18] Z. Zhang, G. Chen, Y. Xue, Q. Duan, X. Liang, T. Lin, Z. Wu, Y. Tan, Q. Zhao, W. Zheng, L. Wang, F. Wang, X. Luo, J. Xu, J. Liu, B. Lu, *Adv. Funct. Mater.* **2023**, *33*, 2305705.
[19] a) M. Hua, S. Wu, Y. Ma, Y. Zhao, Z. Chen, I. Frenkel, J. Strzalka, H. Zhou, X. Zhu, X. He, *Nature* **2021**, *590*, 594–599; b) C. Xiang, Z. Wang, C. Yang, X. Yao, Y. Wang, Z. Suo, *Mater. Today* **2020**, *34*, 7–16; c) J. Kim, G. Zhang, M. Shi, Z. Suo, *Science* **2021**, *374*, 212–216; d) Y. Wu, Y. Zhang, H. Wu, J. Wen, S. Zhang, W. Xing, H. Zhang, H. Xue, J. Gao, Y. Mai, *Adv. Mater.* **2023**, *35*, 2210624.
[20] a) Z. Xu, M. Wu, W. Gao, H. Bai, *Adv. Mater.* **2020**, *32*, 2002695; b) J. Wang, B. Wu, P. Wei, S. Sun, P. Wu, *Nat. Commun.* **2022**, *13*, 4411.
[21] a) S. Chen, L. Sun, X. Zhou, Y. Guo, J. Song, S. Qian, Z. Liu, Q. Guan, E. M. Jeffries, W. Liu, Y. Wang, C. He, Z. You, *Nat. Commun.* **2020**, *11*, 1107; b) W. Yang, V. R. Sherman, B. Gludovatz, E. Schaible, P. Stewart, R. O. Ritchie, M. A. Meyers, *Nat. Commun.* **2015**, *6*, 6649.
[22] J. C. Weaver, G. W. Milliron, A. Miserez, K. Evans-Lutterodt, S. Herrera, I. Gallana, W. J. Mershon, B. Swanson, P. Zavattieri, E. DiMasi, D. Kisailus, *Science* **2012**, *336*, 1275–1280.
[23] J. Ni, S. Lin, Z. Qin, D. Veysset, X. Liu, Y. Sun, A. J. Hsieh, R. Radovitzky, K. A. Nelson, X. Zhao, *Matter* **2021**, *4*, 1919–1934.
[24] Y. Lanir, Y. C. Fung, *J. Biomech.* **1974**, *7*, 29–34.
[25] a) S.-M. Chen, K. Wu, H.-L. Gao, X. Sun, S.-C. Zhang, X.-Y. Li, Z.-B. Zhang, S.-M. Wen, Y. Zhu, H. Wu, Y. Ni, S.-H. Yu, *Matter* **2022**, *5*, 1563–1577; b) Y. Yang, Z. Chen, X. Song, Z. Zhang, J. Zhang, K. K. Shung, Q. Zhou, Y. Chen, *Adv. Mater.* **2017**, *29*, 1605750.
[26] M. Sun, H. Li, Y. Hou, N. Huang, X. Xia, H. Zhu, Q. Xu, Y. Lin, L. Xu, *Sci. Adv.* **2023**, *9*, eade6973.
[27] X. Wei, C. Li, C. McCarthy, J. M. Kolinski, *Nat. Phys.* **2024**, *20*, 1009–1014.
[28] a) S.-M. Wen, S.-M. Chen, W. Gao, Z. Zheng, J.-Z. Bao, C. Cui, S. Liu, H.-L. Gao, S.-H. Yu, *Adv. Mater.* **2023**, *35*, 2211175; b) Y. Chen, B. Dang, J. Fu, J. Zhang, H. Liang, Q. Sun, T. Zhai, H. Li, *ACS Nano* **2022**, *16*, 7525–7534.

Manuscript received: June 18, 2024
Accepted manuscript online: July 10, 2024
Version of record online: September 2, 2024